

Unsupervised-learning-based method for chest MRI–CT transformation using structure constrained unsupervised generative attention networks

Hidetoshi Matsuo, M.D.¹, Mizuho Nishio, M.D., Ph.D.¹, Munenobu Nogami, M.D., Ph.D., FANMB¹, Feibi Zeng, M.D., Ph.D.¹, Takako Kurimoto, Ph.D.², Sandeep Kaushik, MSc.³, Florian Wiesinger, Ph.D.³, Atsushi K Kono, M.D., Ph.D.¹, and Takamichi Murakami, M.D., Ph.D.¹

1 Department of Radiology, Kobe University Graduate School of Medicine, Kobe, Japan

2 GE Healthcare, Hino, Japan

3 GE Healthcare, Munich, Germany

Abstract

The integrated positron emission tomography/magnetic resonance imaging (PET/MRI) scanner facilitates the simultaneous acquisition of metabolic information via PET and morphological information with high soft-tissue contrast using MRI. Although PET/MRI facilitates the capture of high-accuracy fusion images, its major drawback can be attributed to the difficulty encountered when performing attenuation correction, which is necessary for quantitative PET evaluation. The combined PET/MRI scanning requires the generation of attenuation-correction maps from MRI owing to no direct relationship between the gamma-ray attenuation information and MRIs. While MRI-based bone–tissue segmentation can be readily performed for the head and pelvis regions, the realization of accurate bone segmentation via chest CT generation remains a challenging task. This can be attributed to the respiratory and cardiac motions occurring in the chest as well as its anatomically complicated structure and relatively thin bone cortex. This paper presents a means to minimise the anatomical structural changes without human annotation by adding structural constraints using a modality-independent neighbourhood descriptor (MIND) to a generative adversarial network (GAN) that can transform unpaired images. The results obtained in this study revealed the proposed U-GAT-IT + MIND approach to outperform all other competing approaches. The findings of this study hint towards possibility of synthesising clinically acceptable CT images from chest MRI without human annotation, thereby minimising the changes in the anatomical structure.

Keywords

Unsupervised learning, Deep learning, U-GAT-IT, MIND, Chest MRI–CT transformation, PET/MRI

Abbreviations

Deep convolutional neural networks (DCNNs)

Generative adversarial networks (GANs)

Zero echo time (ZTE)

Modality-independent neighbourhood descriptor (MIND)

Positron emission tomography/magnetic resonance imaging (PET/MRI)

1. Introduction

1.1 Background

New methods of machine learning, such as deep convolutional neural networks (DCNNs), have been recently developed because of easy access to large datasets and computational resources, and DCNN has made remarkable progress in various fields. The performance of DCNNs has significantly improved in the field of image recognition research. Generative adversarial networks (GANs) have received considerable attention in neural networks. For example, Zhu et al. developed an unsupervised learning method that enables the transformation of images between two types of domains using GANs called CycleGAN (Goodfellow et al., 2014). They showed that it is possible to transform images between horse and zebra and between day and night (Zhu et al., 2017a).

An integrated positron emission tomography/magnetic resonance imaging (PET/MRI) scanner is the only modality that can obtain metabolic information with PET and morphological information with high soft-tissue contrast using MRI by simultaneous acquisition. Although the advantage of PET/MRI is the accuracy of the fusion images, a major drawback of PET/MRI is the difficulty in attenuation correction for PET reconstruction, which is necessary for the quantitative evaluation of PET. X-ray-based attenuation correction, which is a method of translating CT images from the effective X-ray energy to attenuation coefficients at the PET energy (511 keV), is widely employed for attenuation correction on PET/CT. However, the generation of attenuation correction maps from MRI (a synthesised CT) is necessary for PET/MRI because no direct relationship exists between gamma ray attenuation information and MRIs. Moreover, only four-tissue segmentations (air, lung, fat, and soft tissue) other than bone are used for synthesised CT generation because of the difficulties in extracting signals from tissues with low proton density, such as bone tissue, on conventional MR sequences (Wollenweber et al., 2013).

The zero echo time (ZTE) MR sequence enables imaging of tissues with short T2 relaxation time and is utilised for bone and lung imaging (Gibiino et al., 2015; Grodzki et al., 2012; Madio and Lowe, 1995; Weiger et al., 2011; Wiesinger et al., 2016; Wu et al., 2003). For the head region, ZTE-based attenuation correction is already available in commercial PET/MRI scanners because delineation and segmentation of bone tissue on simultaneously acquired ZTE is relatively easy for rigid and fixed organs (Aasheim et al., 2015; Delso et al., 2015; Sekine et al., 2016; Sgard et al., 2020). A deep learning approach based on the use of paired training data for generating synthesised CT from MRI is now applicable to the head and pelvis

regions (Bradshaw et al., 2018; Leynes et al., 2018; Torrado-Carvajal et al., 2019). In the chest, however, bone segmentation from ZTE remains difficult to perform for accurately synthesised CT generation due to its respiratory and cardiac motion, anatomically complicated structure, and relatively thin cortex of the bone.

Medical image analysis using CycleGAN has been successfully performed, for example, cone-beam-CT-CT conversion (Liang et al., 2019a) and MRI-CT conversion of the head (Lei et al., 2019). In addition to CycleGAN, other types of unsupervised learning methods for interdomain image transformations have been proposed. However, few studies have used these methods in medical image analysis (Tang et al., 2019). In addition, image transformation using GANs faces a problem in that anatomical consistency cannot be guaranteed.

In the current study, to generate synthesised CT from ZTE of PET/MRI, we utilised a new unsupervised method called U-GAT-IT, which is specialised in unpaired image transformation based on attention maps for image transformation (Kim et al., 2019). To guarantee anatomical consistency in the image transformation between different domains (synthesised CT and ZTE), the modality independent neighbourhood descriptor (MIND) (Heinrich et al., 2012) was added to the loss of U-GAT-IT. Using our proposed method, the ZTE of PET/MRI of the chest can be converted to synthesised CT. The U-GAT-IT and CycleGAN models were not originally developed for use in medical image analysis. The anatomical structure might differ significantly in the ZTE and synthesised CT images obtained using the U-GAT-IT or CycleGAN methods. However, to use the synthesised CT as an attenuation correction map for PET/MRI, differences in anatomical structures such as bone, body, and upper arm contour are critical. Our proposed method with U-GAT-IT and MIND successfully prevented anatomical inconsistencies between ZTE and synthesised CT.

1.2 Related works

Transformation in medical images is required in numerous clinical fields, and several applications have been reported, such as noise reduction, MRI-CT transformation, and segmentation tasks. In medical images, however, assembling numerous labelled images for training is challenging. In addition, obtaining an exactly aligned pair of images for intermodality transformation is difficult. Paired training data for the head and pelvis can be prepared by matching the shapes of CT and MRI using nonlinear image registration, whereas prepared such data for the chest is difficult. Although there have been reports on MRI-CT transformation in the head and pelvis, which are relatively unchanged by body posture (Lei et al., 2018; Torrado-Carvajal et al., 2016), it is difficult to obtain an aligned pair of corresponding images of the chest and other regions because of breathing and differences in body posture between MRI and CT. Thus, inter-modality image conversion in the chest has been considered challenging to accomplish.

CycleGAN, which enables unpaired image conversion without the need for directly

corresponding images, has attracted attention. It has performed well in various fields, such as the generation of synthesised CT from cone-beam CT (Liang et al., 2019b), CT segmentation (Sandfort et al., 2019), and X-ray angiography image generation (Tmenova et al., 2019). Generally, CycleGAN is employed to perform transformations between two types of image domains. However, no direct constraint exists on the structure of the input and output images, and the structural alignment between the input and output images is not guaranteed. In medical images, the transforms of the anatomical structures are critical. To overcome this problem, several studies have been performed; CycleGAN has been extended to three-dimensional medical images (Abramian and Eklund, 2019; Cai et al., 2019; Pan et al., 2018), and loss of CycleGAN was changed to set constraints on anatomical structural change (Cai et al., 2019; Wang et al., 2018; Yang et al., 2018). In addition, various approaches have been attempted such as a deformation-invariant CycleGAN (DicycleGAN) (Wang et al., 2018), an extension of CycleGAN by adding the gradient consistency loss to improve the accuracy at the boundaries (Hiasa et al., 2018), and the use of CycleGAN for the paired data (Harms et al., 2019).

1.3 Contributions

The contributions of this study are summarised as follows. First, this paper presents a method for performing chest MRI-CT (ZTE to synthesised CT) transformation using unsupervised learning methods such as U-GAT-IT and CycleGAN, which enable unpaired image transformations. Second, the proposed allows constraints to be applied to U-GAT-IT and CycleGAN to overcome the effect of changes in anatomical structures when transforming chest MRI-CT images. For this purpose, we added MIND to the losses of U-GAT-IT and CycleGAN and attempted to suppress the irregular changes in anatomical structures. (3) The combined use of U-GAT-IT and MIND made it possible to generate clinically acceptable synthesised CT images with less structural changes compared with CycleGAN with and without MIND. (4) Without using any human annotations, the unsupervised learning methods of U-GAT-IT and CycleGAN allowed us to generate synthesised CT.

The remainder of this paper proceeds as follows. Section 2 describes the details of CycleGAN and U-GAT-IT and the loss of these networks using MIND. Section 3 describes the details of PET/MRI and CT imaging and experimental studies used for the performance comparison. Section 4 describes the experimental results. Section 5 discusses the results and compares them with previous studies; finally, the study is concluded in Section 6.

2. Materials and methods

In this study, CycleGAN and U-GAT-IT were used to perform MRI-CT conversion using unpaired data. In addition, we applied MIND, which was proposed in a previous study, to these

networks to prevent misalignment between MRI and synthesised CT images. Please refer to Fig. 1 for an outline of the proposed U-GAT-IT+MIND process.

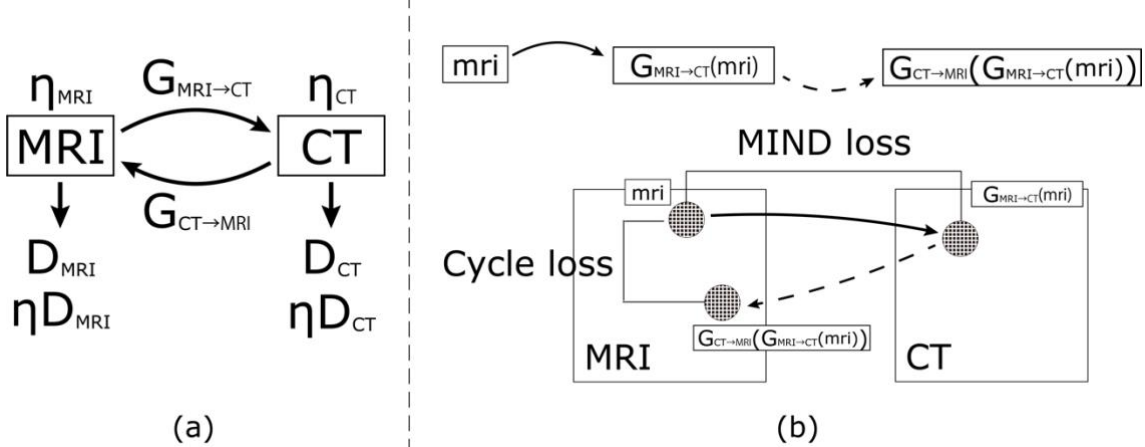


Fig. 1 Outline of proposed U-GAT-IT + MIND process (G , D , and η denote generator, discriminator, and auxiliary classifier, respectively).

To compare the performance of U-GAT-IT + MIND loss, we evaluated the performance of CycleGAN alone, U-GAT-IT alone, and CycleGAN + MIND loss.

2.1 CycleGAN

CycleGAN, developed in 2016, is a method that allows transformations between two different image domains. CycleGAN involves competing networks of an image generator (generator) and an adversarial network (discriminator) that attempt to distinguish the generated synthetic image from the real image. Taking the transformation between MRI and CT images as an example, there is a loss (G loss) to make the synthesised CT image closer to the real CT image for the generator, and a loss (D loss) to distinguish the synthesised CT image from the real CT image for the discriminator. In addition, there are two types of losses in CycleGAN: cycle loss and identity loss. Cycle loss is the difference between the original image and the double-synthesized MRI, which is further synthesised from the synthesised CT based on MRI. Identity loss is the difference between the output image and the input image (CT image and synthesised CT image) when the CT image is input to the CT generator. The same four types of losses are calculated for CT-MRI conversion (when synthesised MRI is generated from real CT). Please refer to the original paper on the conceptual diagram. The four types of losses are as follows:

The equations for generator loss and for the four discriminator types could be expressed as below (equation 1-4).

$$L_{GAN}(G_{MRI \rightarrow CT}, D_{CT}, I_{MRI}, I_{CT}) = \mathbb{E}_{ct \sim p_{data}(I_{CT})} [\log D_{CT}(ct)] + \mathbb{E}_{mri \sim p_{(data)(I_{MRI})}} [\log(1 - D_{CT}(G_{MRI \rightarrow CT}(mri)))] \quad (1)$$

Cycle loss:

$$L_{cyc}(G_{MRI \rightarrow CT}, G_{CT \rightarrow MRI}, I_{MRI}, I_{CT}) = \mathbb{E}_{mri \sim p_{(data)(I_{MRI})}} [\| G_{CT \rightarrow MRI}(G_{MRI \rightarrow CT}(mri)) - mri \|_1] + \mathbb{E}_{ct \sim p_{(data)(I_{CT})}} [\| G_{MRI \rightarrow CT}(G_{CT \rightarrow MRI}(ct)) - ct \|_1] \quad (2)$$

Identity loss:

$$L_{identity}(G_{MRI \rightarrow CT}, G_{CT \rightarrow MRI}, I_{MRI}, I_{CT}) = \mathbb{E}_{ct \sim p_{(data)(I_{CT})}} [\| G_{MRI \rightarrow CT}(ct) - ct \|_1] + \mathbb{E}_{mri \sim p_{(data)(I_{MRI})}} [\| G_{CT \rightarrow MRI}(mri) - mri \|_1] \quad (3)$$

Sum of losses:

$$L_{CycleGAN}(G_{MRI \rightarrow CT}, G_{CT \rightarrow MRI}, D_{MRI}, D_{CT}, I_{MRI}, I_{CT}) = L_{GAN}(G_{MRI \rightarrow CT}, D_{CT}, I_{MRI}, I_{CT}) + L_{GAN}(G_{CT \rightarrow MRI}, D_{MRI}, I_{CT}, I_{MRI}) + \lambda_1 L_{cyc}(G_{MRI \rightarrow CT}, G_{CT \rightarrow MRI}, I_{MRI}, I_{CT}) + \lambda_2 L_{identity}(G_{MRI \rightarrow CT}, G_{CT \rightarrow MRI}, I_{MRI}, I_{CT}) \quad (4)$$

Here, $G_{CT \rightarrow MRI}$ denotes the generator that generates MRI from CT, D_{CT} denotes the discriminator that discriminates between $G_{MRI \rightarrow CT}(mri)$ and ct , and L_{GAN} denotes the loss that includes G loss and D loss. L_{cyc} is the cycle loss, and $L_{identity}$ is the identity loss.

Finally, the model was trained by reducing the losses using equation (5) below.

$$\arg \min_{G_{MRI \rightarrow CT}, G_{CT \rightarrow MRI}} \max_{D_{MRI}, D_{CT}} L_{CycleGAN} \quad (5)$$

2.2 U-GAT-IT

U-GAT-IT is an unsupervised generative attentional network with adaptive layer-instance normalisation for image-to-image translation, which was developed in 2019. Similar to CycleGAN, U-GAT-IT uses the encoder-decoder method for image generation but incorporates the attention module in the discriminator and generator and combines them with the adaptive layer-instance normalisation function (AdaLIN) to focus on the more important parts of the image.

Generator loss and discriminator loss:

$$\begin{aligned} L'_{GAN}(G_{MRI \rightarrow CT}, D_{CT}, I_{MRI}, I_{CT}) &= \mathbb{E}_{ct \sim p_{data}(I_{CT})}[(D_{CT}(ct))^2] \\ &+ \mathbb{E}_{mri \sim p_{data}(I_{MRI})}[(1 - D_{CT}(G_{MRI \rightarrow CT}(mri)))^2] \end{aligned} \quad (6)$$

CAM loss represents the loss that is important for the conversion from MRI and CT based on the information of auxiliary classifiers η_{MRI} and η_{CT} .

CAM losses:

$$\begin{aligned} L_{cam}^{G_{MRI \rightarrow CT}}(G_{MRI \rightarrow CT}, I_{MRI}, I_{CT}, \eta_{MRI}, \eta_{CT}) &= -(\mathbb{E}_{mri \sim p_{data}(I_{MRI})}[\log(\eta_{MRI}(mri))] \\ &+ \mathbb{E}_{ct \sim p_{data}(I_{CT})}[\log(1 - \eta_{CT}(ct))]) \end{aligned} \quad (7)$$

$$\begin{aligned} L_{cam}^{D_{CT}}(G_{MRI \rightarrow CT}, I_{MRI}, I_{CT}, \eta D_{MRI}, \eta D_{CT}) \\ = \mathbb{E}_{ct \sim p_{data}(I_{CT})}[(\eta D_{CT}(ct))^2] + \mathbb{E}_{mri \sim p_{data}(I_{MRI})}[(1 - \eta D_{CT}(G_{MRI \rightarrow CT}(mri)))^2] \end{aligned} \quad (8)$$

Sum of losses:

$$\begin{aligned} L_{U-GAT-IT}(G_{MRI \rightarrow CT}, G_{CT \rightarrow MRI}, D_{MRI}, D_{CT}, I_{MRI}, I_{CT}, \eta_{MRI}, \eta_{CT}, \eta D_{MRI}, \eta D_{CT}) \\ = L'_{GAN}(G_{MRI \rightarrow CT}, D_{CT}, I_{MRI}, I_{CT}) + L'_{GAN}(G_{CT \rightarrow MRI}, D_{MRI}, I_{CT}, I_{MRI}) \\ + \lambda_1 L_{cyc}(G_{MRI \rightarrow CT}, G_{CT \rightarrow MRI}, I_{MRI}, I_{CT}) + \lambda_2 L_{identity}(G_{MRI \rightarrow CT}, G_{CT \rightarrow MRI}, I_{MRI}, I_{CT}) \\ + \lambda_3 L_{cam}^{G_{MRI \rightarrow CT}}(G_{MRI \rightarrow CT}, G_{CT \rightarrow MRI}, I_{MRI}, I_{CT}) + \lambda_3 L_{cam}^{G_{CT \rightarrow MRI}}(G_{CT \rightarrow MRI}, G_{MRI \rightarrow CT}, I_{CT}, I_{MRI}) \\ + \lambda_3 L_{cam}^{D_{MRI}}(G_{MRI \rightarrow CT}, G_{CT \rightarrow MRI}, I_{MRI}, I_{CT}, \eta D_{MRI}, \eta D_{CT}) \\ + \lambda_3 L_{cam}^{D_{CT}}(G_{CT \rightarrow MRI}, G_{MRI \rightarrow CT}, I_{CT}, I_{MRI}, \eta D_{CT}, \eta D_{MRI}) \end{aligned} \quad (9)$$

Here, $G_{CT \rightarrow MRI}$ denotes the generator that generates MRI from CT, D_{CT} denotes the discriminator that discriminates between $G_{MRI \rightarrow CT}(mri)$ and ct , and L'_{GAN} denotes the loss that includes G loss and D loss. $L_{cam}^{G_{MRI \rightarrow CT}}$ is the CAM loss of $G_{MRI \rightarrow CT}$, $L_{cam}^{D_{CT}}$ is the CAM loss of D_{CT} , L_{cyc} is the cycle loss, and $L_{identity}$ is the identity loss. Finally, the model was trained by reducing the losses using the equation (10) below.

$$\arg \min_{G_{MRI \rightarrow CT}, G_{CT \rightarrow MRI}, \eta_{MRI}, \eta_{CT}} \max_{D_{MRI}, D_{CT}, \eta D_{MRI}, \eta D_{CT}} L_{U-GAT-IT} \quad (10)$$

2.3 MIND

MIND is a modality independent neighbourhood descriptor for multi-modal deformable registration reported by Heinrich et al. in 2012 (Heinrich et al., 2012). MIND can extract numerical descriptors preserved across modalities by extracting local feature structures.

$$I_{MIND}(I, x, r) = \frac{1}{n} \exp \left(-\frac{D_p(I, x, x+r)}{V(I, x)} \right) r \epsilon R, \quad (11)$$

where n denotes the normalisation constant (so that the maximum value equals 1), and $r \in R$ defines the region to be calculated; $D_p(I, x, x+r)$ denotes the distance metric between the positions x and $x+r$; it is expressed by the equation (12). In this study, we considered $r = 9$. Calculations were performed by convolution, as in previous studies (Yang et al., 2018). P represents a collection of quantities that shifts the image. In this case, there exist 81 sets that shift the image from -4 to 4 along the X- and Y-axis directions.

$$D_p(I, x, x+r) = \sum_{p \in P} (I(x+p) - I(x+r+p))^2 \quad (12)$$

The denominator $V(I, x)$ represents an estimation of the local variance, and it can be expressed as

$$V(I, x) = \sum_{n \in N} D_p(I, x, x+n), \quad (13)$$

where N denotes the 3-neighbourhood of voxel x . The left image in Fig. 2 presents the original ZTE MRI while the corresponding right image presents MIND. The outlines of the body surface, lungs, bones, and blood vessels in the lungs were extracted.

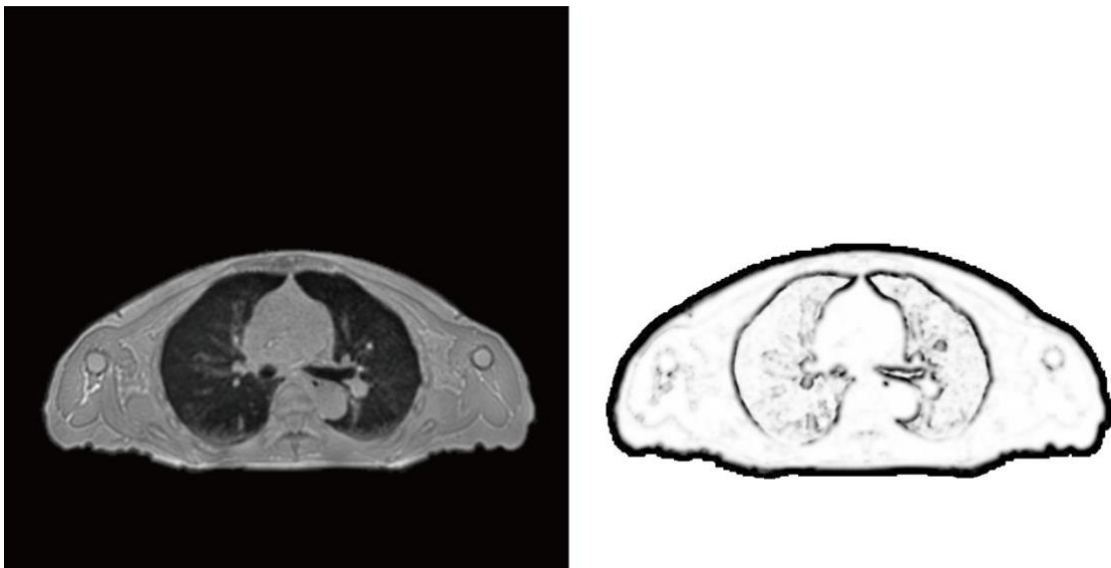


Fig.2 MRI and the corresponding MIND image.

2.3.1 MIND loss

By calculating the MIND on two different images and taking the difference between them, MIND can be used as a loss that adds constraints to the change in position between them. For CycleGAN and U-GAT-IT, the difference between the MIND of the image before and after conversion is used as the loss. The MIND loss is represented by the following equation (14). In the equation, $I_{MIND}(CT, r)$ is the result of adapting MIND to a CT image pixel by pixel.

$$\begin{aligned} & L_{MIND}(G_{MRI \rightarrow CT}, G_{CT \rightarrow MRI}, I_{MRI}, I_{CT}) \\ &= \mathbb{E}_{ct \sim p_{(data)}(I_{CT})} [\| I_{MIND}(G_{CT \rightarrow MRI}(ct), r) - I_{MIND}(ct, r) \|_1] \\ &+ \mathbb{E}_{mri \sim p_{(data)}(I_{MRI})} [\| I_{MIND}(G_{MRI \rightarrow CT}(mri), r) - I_{MIND}(mri, r) \|_1] \end{aligned} \quad (14)$$

By incorporating L_{MIND} into the loss of CycleGAN and U-GAT-IT, constraints to the change in structure can be added. The loss of CycleGAN and U-GAT-IT with the addition of MIND is expressed by the following equations (15-16):

$$\begin{aligned} & L_{CycleGAN+MIND}(G_{MRI \rightarrow CT}, G_{CT \rightarrow MRI}, D_{MRI}, D_{CT}, I_{MRI}, I_{CT}) \\ &= L_{CYCLEGAN} + \lambda_{MIND} L_{MIND}(G_{MRI \rightarrow CT}, G_{CT \rightarrow MRI}, I_{MRI}, I_{CT}) \end{aligned} \quad (15)$$

$$\begin{aligned} & L_{U-GAT-IT+MIND}(G_{MRI \rightarrow CT}, G_{CT \rightarrow MRI}, D_{MRI}, D_{CT}, I_{MRI}, I_{CT}, \eta_{MRI}, \eta_{CT}, \eta D_{MRI}, \eta D_{CT}) \\ &= L_{U-GAT-IT} + \lambda_{MIND} L_{MIND}(G_{MRI \rightarrow CT}, G_{CT \rightarrow MRI}, I_{MRI}, I_{CT}) \end{aligned} \quad (16)$$

Finally, models are trained by reducing loss in equation (17) and (18).

$$\arg \min_{G_{MRI \rightarrow CT}, G_{CT \rightarrow MRI}} \max_{D_{MRI}, D_{CT}} L_{CycleGAN+MIND} \quad (17)$$

$$\arg \min_{G_{MRI \rightarrow CT}, G_{CT \rightarrow MRI}, \eta_{MRI}, \eta_{CT}} \max_{D_{MRI}, D_{CT}, \eta D_{MRI}, \eta D_{CT}} L_{U-GAT-IT+MIND} \quad (18)$$

3. Experiments

This study conformed to the Declaration of Helsinki and the Ethical Guidelines for Medical and Health Research Involving Human Subjects in Japan (<https://www.mhlw.go.jp/stf/seisaku-jouhou-10600000-daijinkanboukouseikagakuka/0000080278.pdf>). The requirement for informed consent was waived because of the retrospective design. This study was approved by the ethical committee and was carried out according to the guidelines of the committee.

3.1 In-phase ZTE acquisition on PET/MRI

All PET/MRI examinations ($n = 150$; mean age, 65.9 ± 13.0 years ; range 19 to 90 years) were performed on an integrated PET/MRI scanner (SIGNA PET/MR, GE Healthcare, Waukesha, WI, USA) at 3.0 T magnetic field strength. MR imaging of the thoracic bed position was performed with the ZTE sequence and was simultaneously acquired with a PET emission scan. No contrast-enhancing material was used. Free-breathing ZTE was acquired by three-dimensional (3D) centre-out radial sampling to provide an isotropic resolution of $(2\text{mm})^3$, large field of view of $(50\text{ cm})^3$, and a minimal TE of zero with the following parameters: TR, $\sim 1.4\text{ms}$; FA, 1° ; 250000 radial centre-out spokes; matrix size, 250×250 ; FOV, $(50.0\text{ cm})^3$; resolution, $(2\text{mm})^3$; number of spokes per segment, 512; and approximate acquisition time, 5 min. To minimize, fat-water chemical shift effects (i.e. destructive interference at fat-water tissue boundaries), a high imaging bandwidth of ± 62.5 kHz was used. Furthermore, the imaging centre frequency was adjusted to be between fat and water resulting in clean in-phase ZTE images with uniform soft-tissue signal response and minimal fat-water interference disturbances (Brodsky et al., 2008; Engström et al., 2020).

3.2 CT component of PET/CT

The CT component of PET/CT (Discovery PET/CT 690 (GE Healthcare), number of scans = 150; mean age, 64.4 ± 13.9 years ; range, 12–86 years) was utilised for training the CT data. The training data of ZTE and CT were acquired from different patients (unpaired datasets); however, ZTE and CT were performed in the same body position (arms down) on the respective scanners. CT was acquired during shallow expiratory breath-holding for attenuation correction of PET and acquisition of anatomical details with the following parameters: X-ray tube peak voltage (kVp), 120 kV; tube current, 20 mA; section thickness, 3.27 mm; reconstructed diameter, 500 mm; reconstructed convolutional kernel, soft.

3.3 Dataset splitting

Data of thirty cases (20%) were used as the validation dataset, and data of the remaining 120 cases (80%) were used as the training dataset. For each case, unpaired CT and ZTE were used, and no manual annotations were performed.

3.4 Image postprocessing

ZTE images were semi-automatically processed to remove the background signals by using a thresholding and filling-in technique on a commercially available workstation (Advantage workstation, GE Healthcare) and converted into a matrix size of 640×400 . To correct the variations in sensitivity and normalise the images of ZTE to the median tissue value, the nonparametric N4ITK method was applied (Sled et al., 1998; Tustison et al., 2010). CT images were also modified to remove

the scanner beds on the workstation and were converted into the same matrix size. The MRI was maintained at the window width and window level stored in DICOM images, whereas the CT image was adjusted to a window width of 2000 Hounsfield Unit (HU) and a window level of 350 HU. The CT images were then scaled down to an image resolution of 256×256 pixels owing to GPU memory limitations.

3.5 Model training

All processing was performed using a workstation (CPU: Core i7-9800X at 3.80 GHz, RAM 64 GB, GPU: TITAN RTX) in all cases of CycleGAN, CycleGAN+MIND, U-GAT-IT, and U-GAT-IT+MIND.

3.5.1 *CycleGAN / CycleGAN+MIND*

We used a program based on the PyTorch implementation of CycleGAN (Zhu et al., 2017b), which was modified for DICOM images and MIND calculations. We used values of 10, 0.5, and 20 for λ_1 , λ_2 , and λ_{MIND} , respectively, in CycleGAN+MIND with Adam as the optimizer and a learning rate of 0.0002 up to 1000 epochs. A radiologist (4 years experiment) visually evaluated the results when the loss reached equilibrium. If no corruption of synthesised CT was confirmed for the training and validation datasets, the trained network was used for the main visual evaluation described below. Except λ_{MIND} , the hyperparameters of CycleGAN and CycleGAN+MIND were the same.

3.5.2 *U-GAT-IT / U-GAT-IT+MIND*

We used a program based on the PyTorch implementation of U-GAT-IT (Kim et al., 2019), which was modified for DICOM images and MIND calculations. We used 100 for λ_1 , 100 for λ_2 , 100 for λ_3 , and 5000 for λ_{MIND} in U-GAT-IT +MIND, with Adam as the optimizer and a learning rate of 0.0001 up to 100 epochs. The results when the loss reached equilibrium and the training data were not corrupted by visual confirmation by the radiologist were used for evaluation. Except λ_{MIND} , the hyperparameters of U-GAT-IT and U-GAT-IT+MIND were the same.

3.6 Visual evaluation

Twenty-one cases of chest ZTE unused for the training and validation datasets were prepared as the test dataset. The test dataset did not contain any CT images. The synthesised CTs were calculated using CycleGAN, CycleGAN+MIND, U-GAT-IT, and U-GAT-IT+MIND based on axial cross-sectional ZTE images of the supraclavicular fossa, central humeral head, sternoclavicular joint,

aortic arch, tracheal bifurcation, and right pulmonary vein levels in each case. In this study, the main purpose was the application of PET/MRI attenuation correction maps; therefore, it was particularly important to suppress the difference in anatomical structure during the conversion. For this purpose, two radiologists evaluated the synthesised CT visually, as shown below. Before evaluation by the two radiologists, a radiologist (15-year experiments) evaluated the synthesised CT images, and almost all of them were rated as CT-like for CycleGAN, CycleGAN+MIND, U-GAT-IT, and U-GAT-IT+MIND.

3.6.1 Evaluation of image misalignment after conversion

Visual evaluation was performed by two radiologists (Dr. A, a radiologist with 4 years of experience, and Dr. B, a radiologist with 22 years of experience). The alignment between the synthesised CTs and the original images of the ZTE was visually evaluated for bone structures. When a relatively large defect, large displacement, or large deformation of the shape of the bone structures were observed, they were classified as severe misalignment. When a relatively small defect, small displacement, or small deformation of the shape of the bone structures were observed, they were classified as minor misalignment. One point was given when a total of 10 or more major misalignments were found in six images; two points when a total of five or more major misalignments were found; 3 points when a total of three or more major misalignments or 15 or more minor misalignments were found; 4 points when a total of 1 or more major misalignments or 10 or more minor misalignments were found; and 5 points for the others.

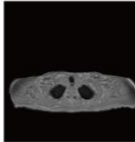
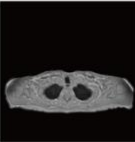
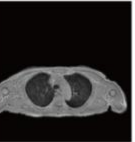
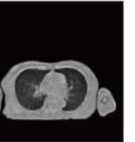
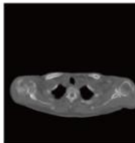
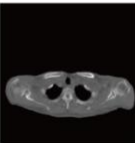
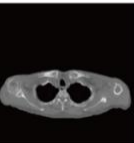
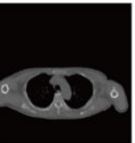
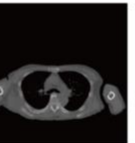
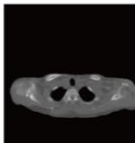
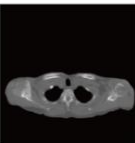
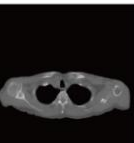
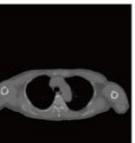
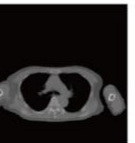
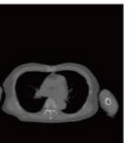
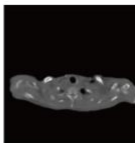
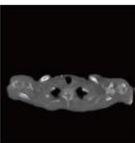
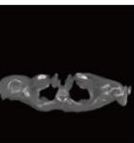
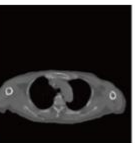
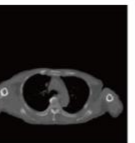
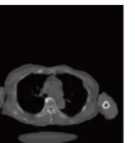
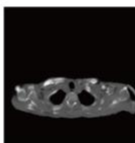
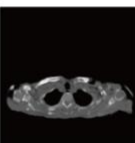
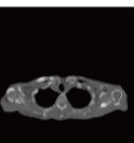
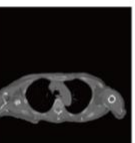
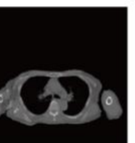
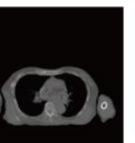
3.7 Statistics

The U-GAT-IT+MIND and other groups were compared using the Wilcoxon signed-rank test to evaluate the visual evaluation scores of the two radiologists. The Bonferroni method was used to correct multiple comparisons, and statistical significance was set at $p<0.002$.

4. Results

4.1 Synthesized CT

In Figs. 3 and 4, the images on the top are MRI images, and those on the second to fifth rows are the synthesised CTs. Figs. 3b and 4b show fused images obtained from MRI and synthesised CT.

	Patient 1						Score
Original MR							
CycleGAN							Dr.A - 1 Dr.B - 2
CycleGAN+MIND							Dr.A - 3 Dr.B - 3
U-GAT-IT							Dr.A - 1 Dr.B - 1
U-GAT-IT+MIND							Dr.A - 5 Dr.B - 5

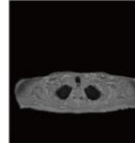
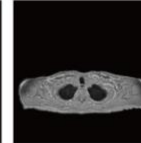
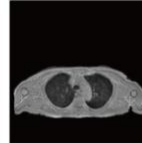
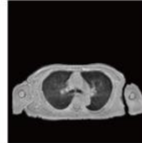
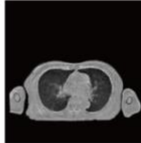
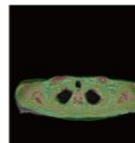
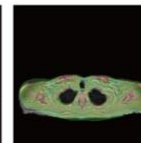
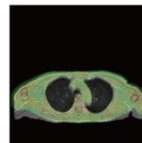
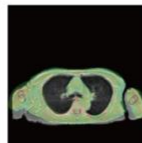
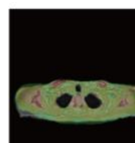
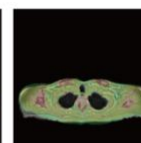
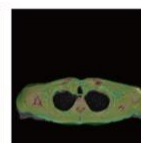
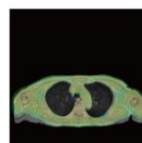
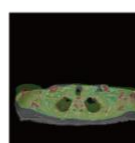
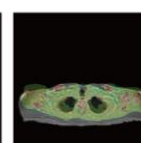
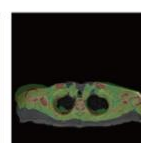
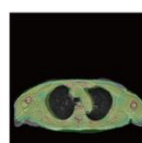
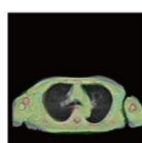
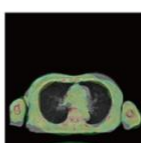
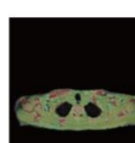
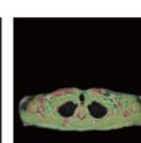
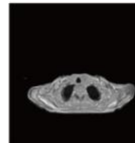
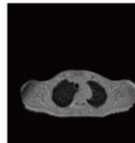
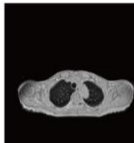
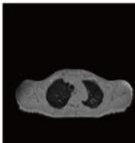
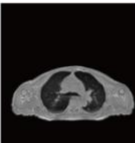
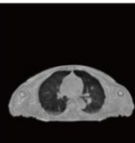
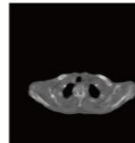
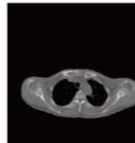
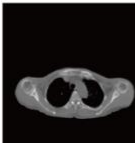
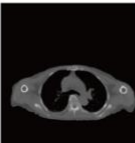
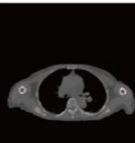
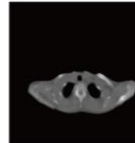
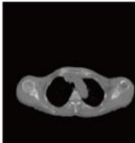
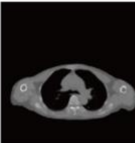
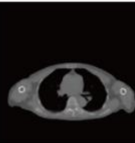
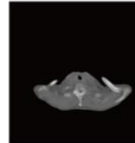
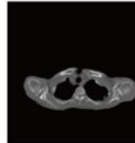
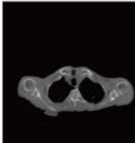
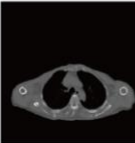
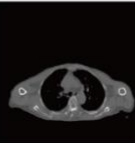
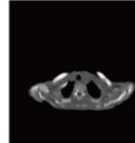
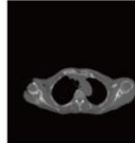
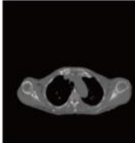
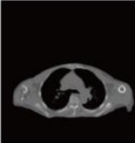
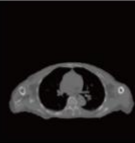
	Patient 1						Score
Original MR							
CycleGAN							Dr.A - 1 Dr.B - 2
CycleGAN+MIND							Dr.A - 3 Dr.B - 3
U-GAT-IT							Dr.A - 1 Dr.B - 1
U-GAT-IT+MIND							Dr.A - 5 Dr.B - 5

Fig. 3a-b Original MR image, synthesized CT image, and visual evaluation scores of Patient 1.

	Patient 2						Score
Original MR							
CycleGAN							Dr.A - 3 Dr.B - 3
CycleGAN+MIND							Dr.A - 3 Dr.B - 3
U-GAT-IT							Dr.A - 3 Dr.B - 3
U-GAT-IT+MIND							Dr.A - 5 Dr.B - 5

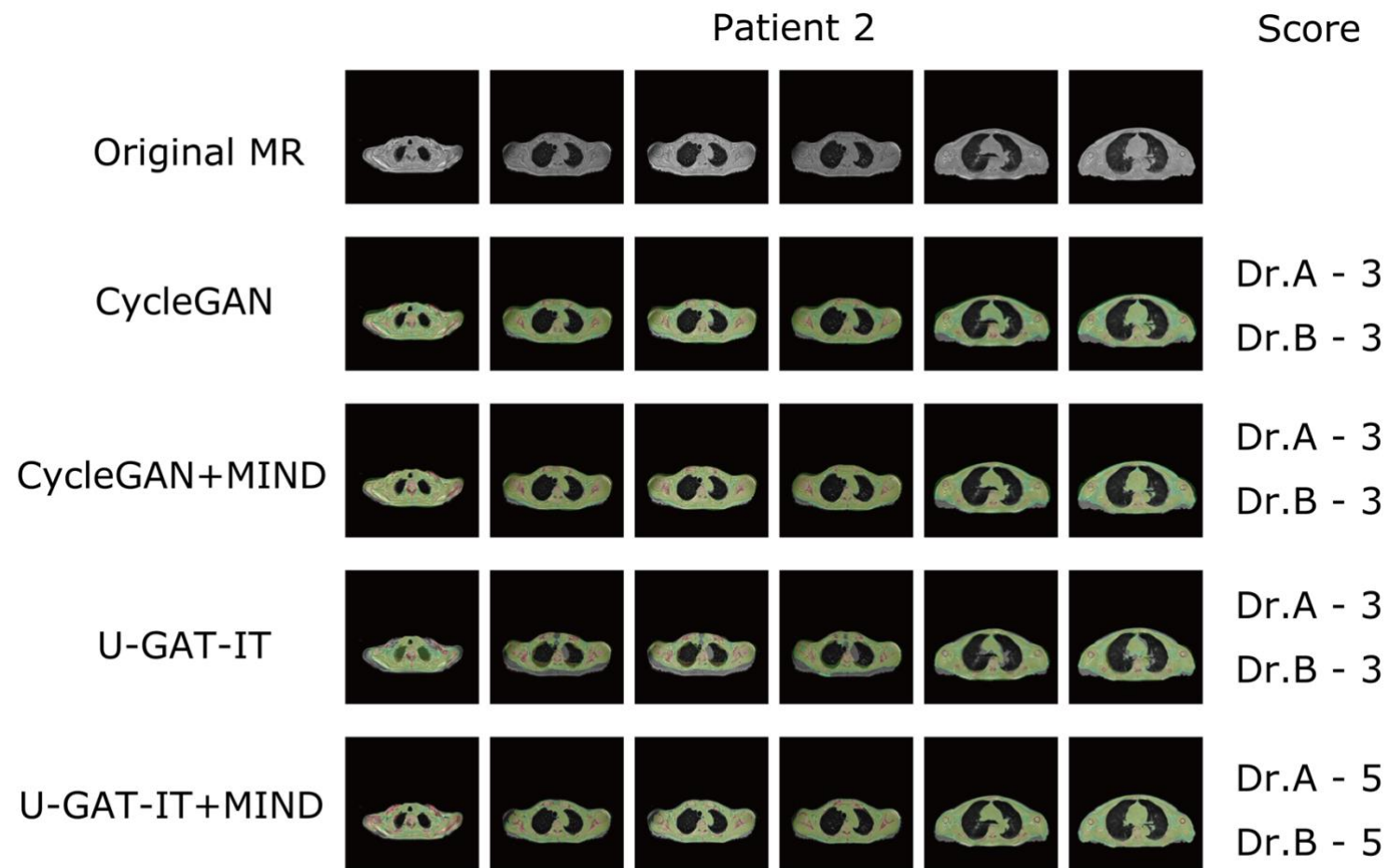


Fig. 4a-b Original MR image, synthesized CT image, and visual evaluation scores of Patient 2.

Fig. 5 shows the 3D VR images of the front and side views compositing from the synthesised CT.

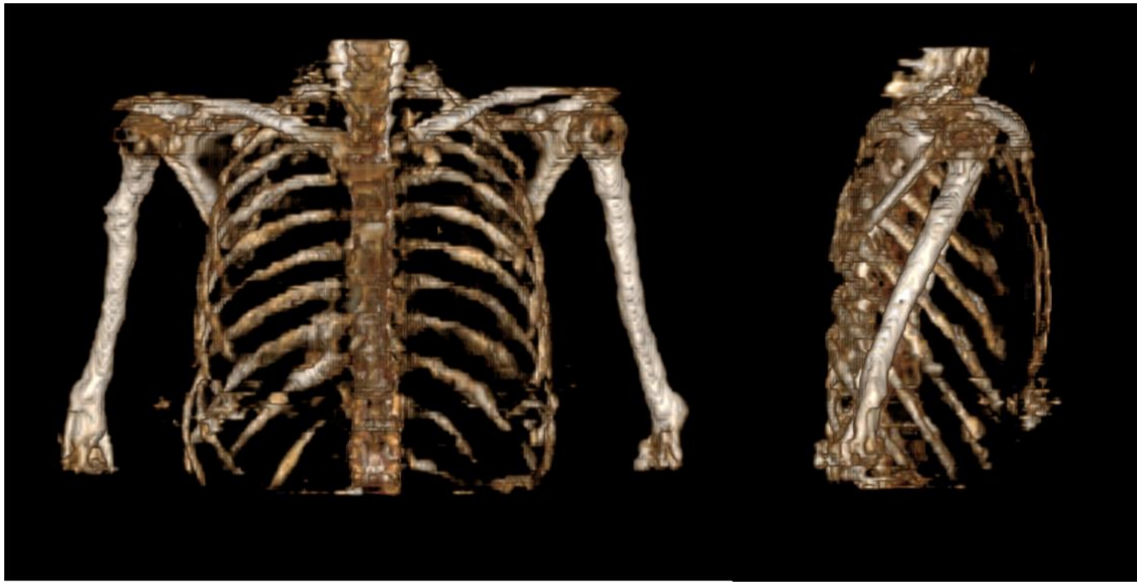


Fig. 5 Three-dimensional VR images of bones obtained from synthesized CT.

The upper row of Fig. 6 shows the synthesised CT based on the combination of the proposed method and conventional four-tissue segmentation, and the lower row shows the synthesised CT based on conventional four-tissue segmentation. The latter is clinically used for attenuation correction of PET/MRI. The upper row shows bone structures, which could not be synthesized with the conventional synthetic method.

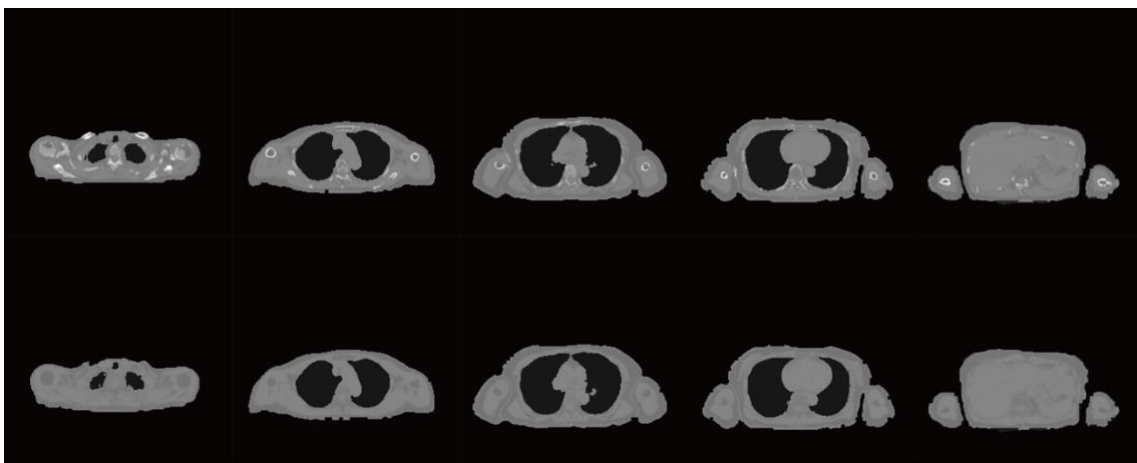


Fig. 6 Synthesized CTs using U-GAT-IT+MIND and conventional method.

The upper row shows the combination of U-GAT-IT+MIND and conventional four-tissue segmentation. The lower row shows the synthesised CT based on the conventional four-tissue segmentation.

4.2 Visual evaluation

The results of visual evaluation could be described in terms of the below scores.

- CycleGAN: maximum = 4, minimum = 1, and median = 2 by Dr. A and maximum = 4, minimum = 2, and median = 3 by Dr. B
- CycleGAN + MIND: maximum = 4, minimum = 1, and median = 2 by Dr. A and maximum = 4, minimum = 2, and median = 3 by Dr. B
- U-GAT-IT: maximum = 3, minimum = 1, and median = 1 by Dr. A and maximum = 4, minimum = 1, and median = 3 by Dr. B
- U-GAT-IT + MIND: maximum = 5, minimum = 3, and median = 5 by Dr. A and maximum = 5, minimum = 3, and median = 5 by Dr. B

Figs. 7(a) and 8(b) show the distribution of visual evaluation scores by radiologists for CycleGAN, CycleGAN+MIND, U-GAT-IT, and U-GAT-IT+MIND. The boxplot of the scores of the four groups is shown in Fig. 9, and the pair plot is shown in Figs. 10 and 11.

The results of the Wilcoxon signed-rank test showed that U-GAT-IT+MIND was significantly better than CycleGAN, CycleGAN+MIND, and U-GAT-IT. (Dr. A, $p < 0.00001$, $p < 0.00001$, $p < 0.00001$; Dr. B, $p = 0.00008$, $p = 0.00008$, $p < 0.00001$, respectively)

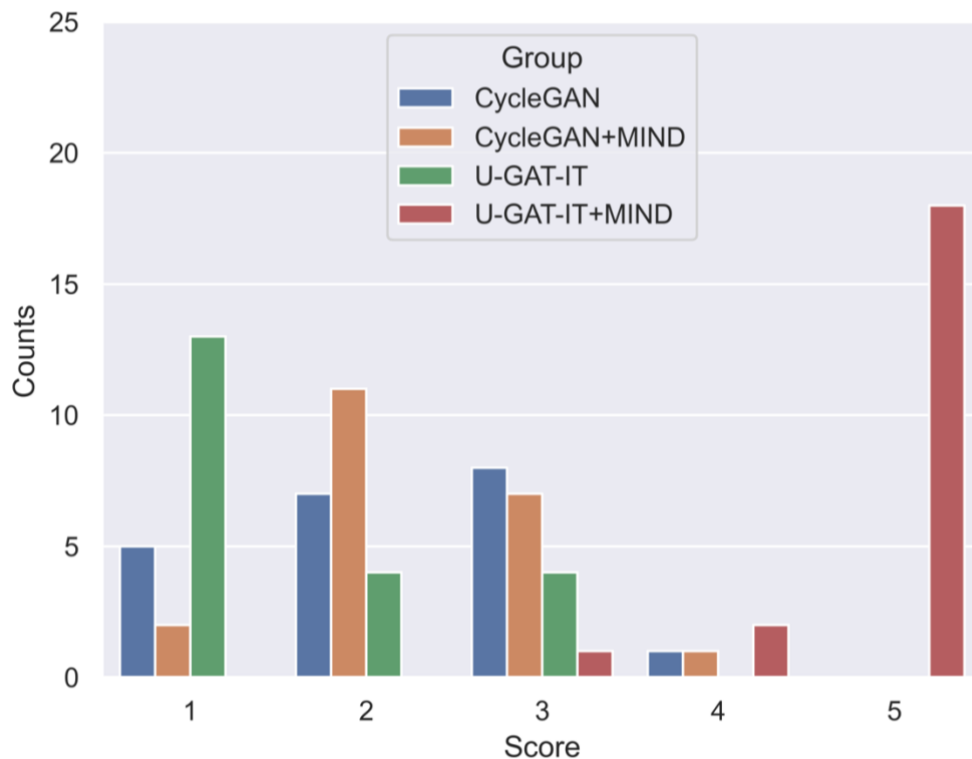


Fig.7 Distribution of the evaluation scores of the four groups by Dr. A

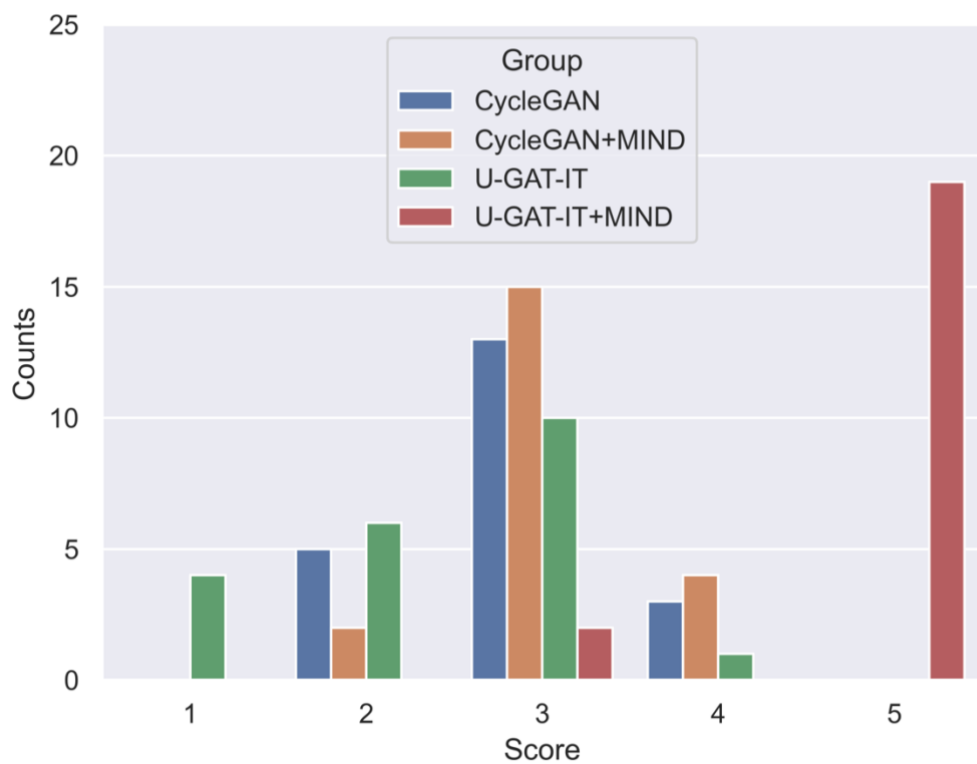


Fig.8 Distribution of the evaluation scores of the four groups by Dr. B

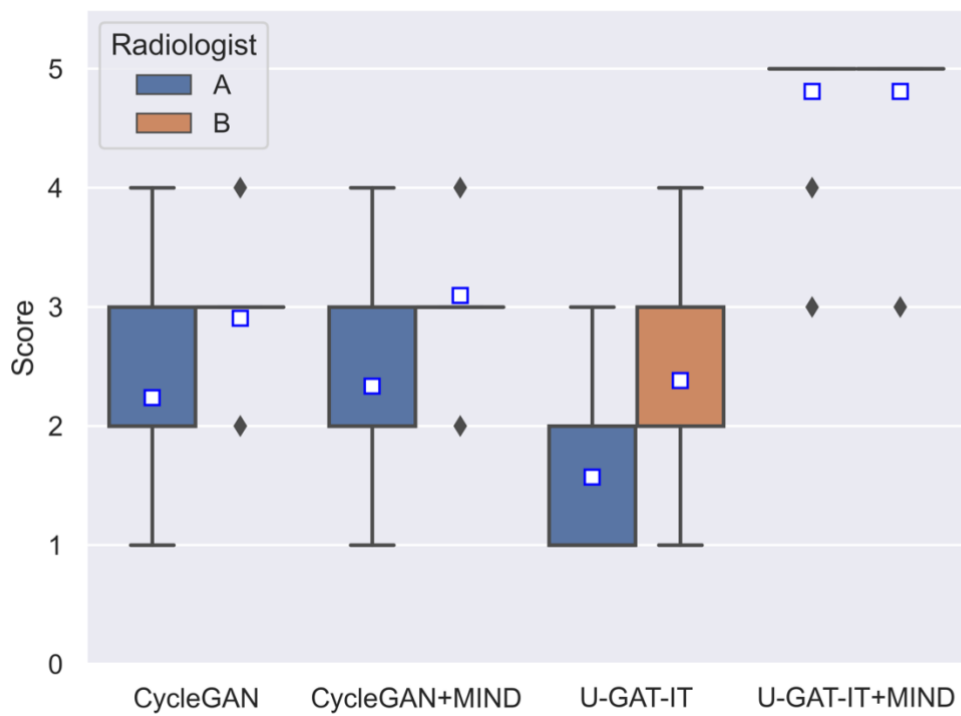


Fig.9 Boxplot of visual evaluation scores

The square indicates the median score. U-GAT-IT+MIND showed a tendency to score higher for both Dr. A and Dr. B.

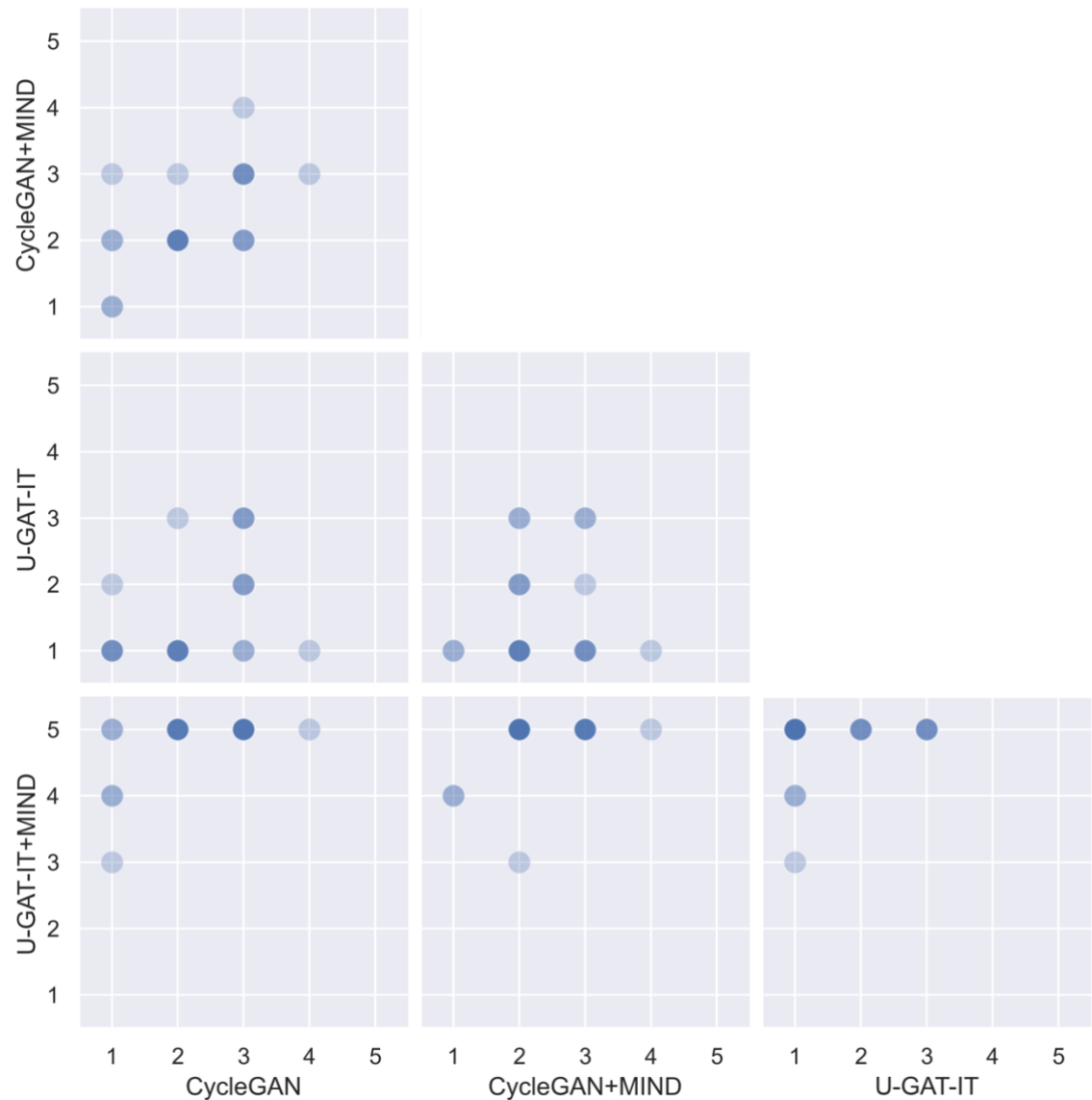


Fig. 10 Pair-plot of visual-evaluation scores (Dr. A) (dark circles indicate high frequencies)

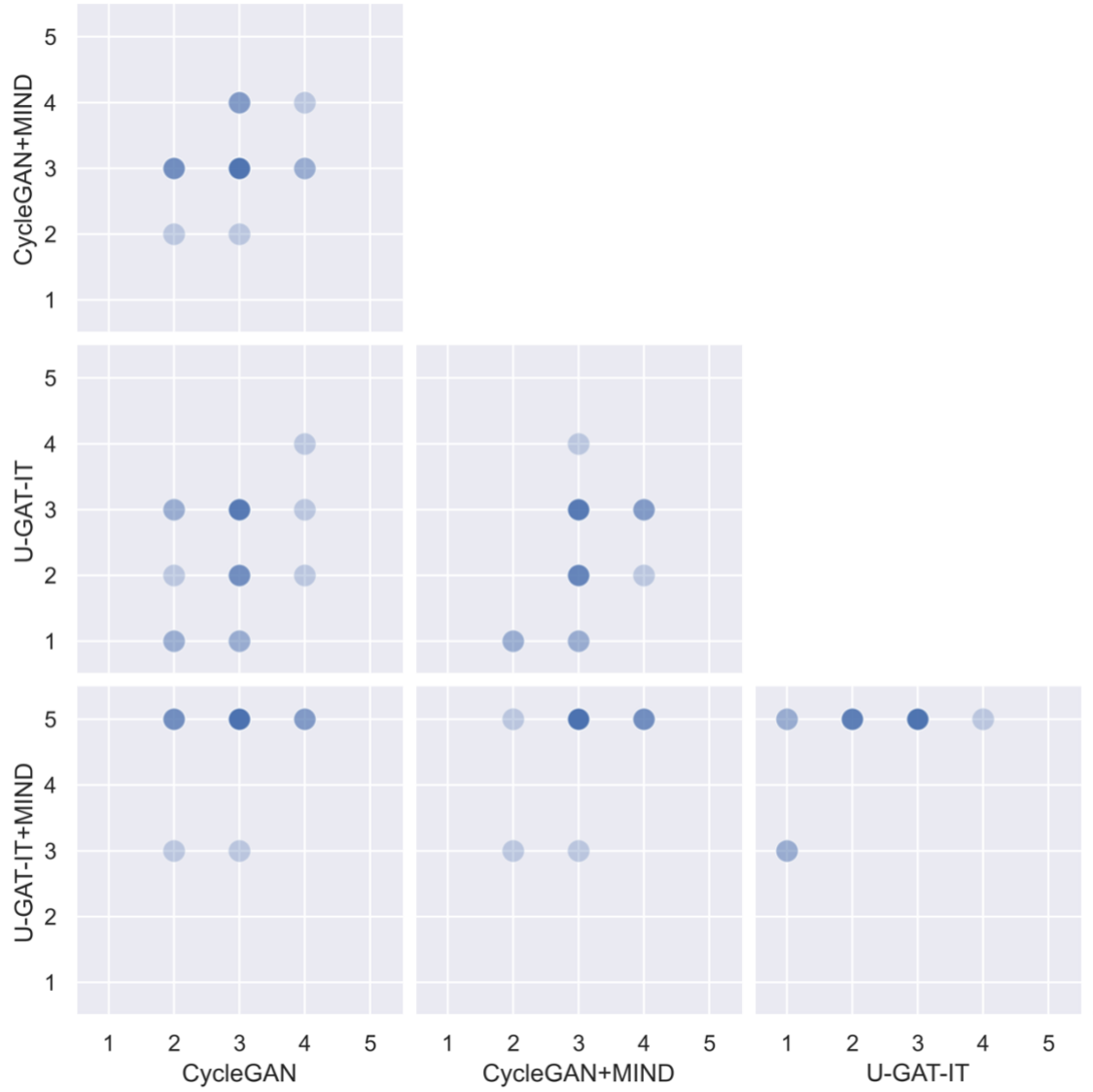


Fig. 11 Pair-plot of visual-evaluation scores (Dr. B) (dark circles indicate high frequencies)

4.3 CycleGAN+MIND with high coefficient of MIND loss

The larger the coefficient of MIND loss in CycleGAN+MIND, the more collapsed the synthesised CT became, thus distorting its contrast. Fig. 12 shows the synthesised CTs from CycleGAN+MIND with a high coefficient of MIND loss ($\lambda_{MIND} = 60$), which were apparently different from those of a normal CT. Thus, the coefficients of MIND loss of CycleGAN+MIND could not be increased to the same value as the coefficients of MIND loss of U-GAT-IT+MIND. These images depicted in Fig. 12 below appear different when captured via normal CT.

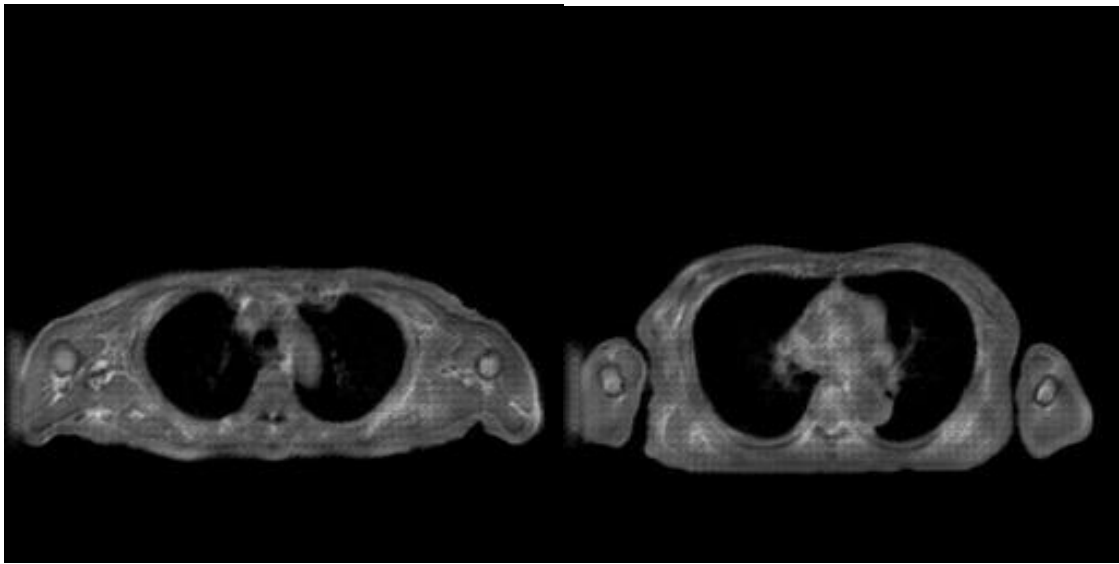


Fig.12 a-b CT images synthesized using CycleGAN + MIND with high MIND loss coefficient
These images were apparently different in contrast to a normal CT.

5. Discussion

The combination of U-GAT-IT and MIND can help in image conversion between MRI and CT images with smaller misregistration compared to conventional unpaired image transfer (CycleGAN) using unpaired datasets. The generation of paired datasets for training is simple for the head, neck, and pelvis regions because changes in body position and deformation of organs between different scans are anatomically small, which allows simple non-rigid registrations to adjust the paired data in the hand, neck, or pelvis regions. However, in the chest region, manual annotations or registrations are required to generate the paired datasets, which makes the process extremely time-consuming; furthermore, such models lack robustness because of the anatomically complicated structures of the chest and significant changes and deformation of the images between scans due to different respiratory motions, different scanner-bed shapes, and different body positions, which were the strong motivators to develop an unsupervised method for image conversion with unpaired datasets in this study. Because the annotation of bone structures is not practically possible for the chest region, it is difficult to perform quantitative evaluation; hence, visual evaluations were performed.

In this work, we also tried the combination of CycleGAN and MIND; however, the generated images were apparently different in contrast to a normal CT when the coefficient of loss by MIND (λ_{MIND}) was increased to the same range as that used for U-GAT-IT+MIND. the CAM loss introduced in U-GAT-IT prevents inconsistencies caused by the increase in MIND loss. When the coefficients of CAM loss were reduced without changing the other coefficients, the generated images seemed not to be CT-like in contrast, suggesting that the effect of CAM loss on the conversion between images was important.

There are some limitations to our study. First, we did not evaluate the effect of the synthesised CT on PET accumulation in this study. Further studies are required to confirm this hypothesis. Second, our study was conducted with a single PET/MRI scanner at a single institution, and external validation was not performed. Because the number of distributed PET/MRI scanners is limited, external validation with multiple PET/MRI scanners is difficult. Because both CycleGAN and U-GAT-IT are image conversion techniques based on unsupervised learning, the effect of overfitting is expected to be low.

6. Conclusions

The combination of U-GAT-IT and MIND was effective in preventing anatomical inconsistencies between ZTE and synthesised CT and enabled the generation of clinically acceptable synthesised CT images. Our method also enables inter-modality image conversion in the chest region, which has been challenging to accomplish up until now without using human annotations.

Acknowledgement

This work was supported by JSPS KAKENHI (Grant Number JP20K16758).

References

Aasheim, L.B., Karlberg, A., Goa, P.E., Håberg, A., Sørhaug, S., Fagerli, U.M., Eikenes, L., 2015. PET/MR brain imaging: evaluation of clinical UTE-based attenuation correction. *Eur. J. Nucl. Med. Mol. Imaging*. 42, 1439–1446. <https://doi.org/10.1007/s00259-015-3060-3>

Abramian, D., Eklund, A., 2019. Generating fMRI volumes from T1-weighted volumes using 3D CycleGAN. *Bradshaw, T.J., Zhao, G., Jang, H., Liu, F., McMillan, A.B., 2018. Feasibility of Deep Learning-Based PET/MR Attenuation Correction in the Pelvis Using Only Diagnostic MR Images. Tomography* 4, 138–147. <https://doi.org/10.18383/j.tom.2018.00016>

Brodsky, E.K., Holmes, J.H., Yu, H., Reeder, S.B., 2008. Generalized K-space decomposition with chemical shift correction for non-Cartesian water-fat imaging. *Magn. Reson. Med.* 59, 1151–1164. <https://doi.org/10.1002/mrm.21580>

Cai, J., Zhang, Z., Cui, L., Zheng, Y., Yang, L., 2019. Towards cross-modal organ translation and segmentation: A cycle- and shape-consistent generative adversarial network. *Med. Image Anal.* 52, 174–184. <https://doi.org/10.1016/j.media.2018.12.002>

Delso, G., Wiesinger, F., Sacolick, L.I., Kaushik, S.S., Shanbhag, D.D., Hüllner, M., Veit-Haibach, P., 2015. Clinical evaluation of zero-echo-time MR imaging for the segmentation of the skull. *J. Nucl. Med.* 56, 417–422. <https://doi.org/10.2967/jnumed.114.149997>

Engström, M., McKinnon, G., Cozzini, C., Wiesinger, F., 2020. In-phase zero TE musculoskeletal imaging. *Magn. Reson. Med.* 83, 195–202. <https://doi.org/10.1002/mrm.27928>

Gibino, F., Sacolick, L., Menini, A., Landini, L., Wiesinger, F., 2015. Free-breathing, zero-TE MR lung imaging. *Magnetic Resonance Materials in Physics, Biology and Medicine* 28, 207–215. <https://doi.org/10.1007/s10334-014-0459-y>

Goodfellow, I.J., Pouget-Abadie, J., Mirza, M., Xu, B., Warde-Farley, D., Ozair, S., Courville, A., Bengio, Y., 2014. Generative Adversarial Nets, *Advances in Neural Information Processing Systems*.

Grodzki, D.M., Jakob, P.M., Heismann, B., 2012. Correcting slice selectivity in hard pulse sequences. *J. Magn. Reson.* 214, 61–67. <https://doi.org/10.1016/j.jmr.2011.10.005>

Harms, J., Lei, Y., Wang, T., Zhang, R., Zhou, J., Tang, X., Curran, W.J., Liu, T., Yang, X., 2019. Paired cycle-GAN-based image correction for quantitative cone-beam computed tomography. *Med. Phys.* 46, 3998–4009. <https://doi.org/10.1002/mp.13656>

Heinrich, M.P., Jenkinson, M., Bhushan, M., Matin, T., Gleeson, F. V., Brady, S.M., Schnabel, J.A., 2012. MIND: Modality independent neighbourhood descriptor for multi-modal deformable registration. *Med. Image Anal.* 16, 1423–1435. <https://doi.org/10.1016/j.media.2012.05.008>

Hiasa, Y., Otake, Y., Takao, M., Matsuoka, T., Takashima, K., Carass, A., Prince, J.L., Sugano, N., Sato, Y., 2018. Cross-modality image synthesis from unpaired data using cyclegan: Effects of gradient consistency loss and training data size, in: *Lecture Notes in Computer Science (Including Subseries Lecture Notes in Artificial Intelligence)* 10713, 142–153. https://doi.org/10.1007/978-3-030-00072-6_13

in Artificial Intelligence and Lecture Notes in Bioinformatics). Springer Verlag, pp. 31–41. https://doi.org/10.1007/978-3-030-00536-8_4

Kim, J., Kim, M., Kang, H., Lee, K., 2019. U-GAT-IT: Unsupervised Generative Attentional Networks with Adaptive Layer-Instance Normalization for Image-to-Image Translation.

Kläser, K., Varsavsky, T., Markiewicz, P., Vercauteren, T., Hammers, A., Atkinson, D., Thielemans, K., Hutton, B., Cardoso, M.J., Ourselin, S., 2021. Imitation learning for improved 3D PET/MR attenuation correction. *Med. Image Anal.* 71, 102079. <https://doi.org/10.1016/j.media.2021.102079>

Lei, Y., Harms, J., Wang, T., Liu, Y., Shu, H., Jani, A.B., Curran, W.J., Mao, H., Liu, T., Yang, X., 2019. MRI-only based synthetic CT generation using dense cycle consistent generative adversarial networks. *Med. Phys.* 46, 3565–3581. <https://doi.org/10.1002/mp.13617>

Lei, Y., Jeong, J.J., Wang, T., 2018. MRI-based pseudo CT synthesis using anatomical signature and alternating random forest with iterative refinement model. *J. Med. Imaging* 5, 1. <https://doi.org/10.1117/1.jmi.5.4.043504>

Leynes, A.P., Yang, J., Wiesinger, F., Kaushik, S.S., Shanbhag, D.D., Seo, Y., Hope, T.A., Larson, P.E.Z., 2018. Zero-echo-time and dixon deep pseudo-CT (ZeDD CT): Direct generation of pseudo-CT images for Pelvic PET/MRI Attenuation Correction Using Deep Convolutional Neural Networks with Multiparametric MRI. *J. Nucl. Med.* 59, 852–858. <https://doi.org/10.2967/jnumed.117.198051>

Liang, X., Chen, L., Nguyen, D., Zhou, Z., Gu, X., Yang, M., Wang, J., Jiang, S., 2019a. Generating synthesized computed tomography (CT) from cone-beam computed tomography (CBCT) using CycleGAN for adaptive radiation therapy. *Phys. Med. Biol.* 64, 125002. <https://doi.org/10.1088/1361-6560/ab22f9>

Madio, D.P., Lowe, I.J., 1995. Ultra-fast imaging using low flip angles and fids. *Magn. Reason. Med.* 34, 525–529. <https://doi.org/10.1002/mrm.1910340407>

Pan, Y., Liu, M., Lian, C., Zhou, T., Xia, Y., Shen, D., 2018. Synthesizing missing PET from MRI with cycle-consistent generative adversarial networks for Alzheimer’s disease diagnosis, in: Lecture Notes in Computer Science (Including Subseries Lecture Notes in Artificial Intelligence and Lecture Notes in Bioinformatics). Springer Verlag, pp. 455–463. https://doi.org/10.1007/978-3-030-00931-1_52

Sandfort, V., Yan, K., Pickhardt, P.J., Summers, R.M., 2019. Data augmentation using generative adversarial networks (CycleGAN) to improve generalizability in CT segmentation tasks. *Sci. Rep.* 9, 16884. <https://doi.org/10.1038/s41598-019-52737-x>

Sekine, T., Ter Voert, E.E.G.W., Warnock, G., Buck, A., Huellner, M., Veit-Haibach, P., Delso, G., 2016. Clinical evaluation of zero-echo-time attenuation correction for brain 18F-FDG PET/MRI: Comparison with atlas attenuation correction. *J. Nucl. Med.* 57, 1927–1932. <https://doi.org/10.2967/jnumed.116.175398>

Sgard, B., Khalifé, M., Bouchut, A., Fernandez, B., Soret, M., Giron, A., Zaslavsky, C., Delso, G., Habert, M.O., Kas, A., 2020. ZTE MR-based attenuation correction in brain FDG-PET/MR: performance in patients

with cognitive impairment. *Eur. Radiol.* 30, 1770–1779. <https://doi.org/10.1007/s00330-019-06514-z>

Sled, J.G., Zijdenbos, A.P., Evans, A.C., 1998. A nonparametric method for automatic correction of intensity nonuniformity in mri data. *IEEE Trans. Med. Imaging.* 17, 87–97. <https://doi.org/10.1109/42.668698>

Tang, Youbao, Tang, Yuxing, Xiao, J., Summers, R.M., 2019. XLSor: A Robust and Accurate Lung Segmentor on Chest X-Rays Using Criss-Cross Attention and Customized Radiorealistic Abnormalities Generation.

Tmenova, O., Martin, R., Duong, L., 2019. CycleGAN for style transfer in X-ray angiography. *Int. J. Comput. Assist. Rad. Surg.* 14, 1785–1794. <https://doi.org/10.1007/s11548-019-02022-z>

Torrado-Carvajal, A., Herranz, J.L., Alcain, E., Montemayor, A.S., Garcia-Canamaque, L., Hernandez-Tamames, J.A., Rozenholc, Y., Malpica, N., 2016. Fast patch-based pseudo-CT synthesis from T1-weighted MR images for PET/MR attenuation correction in brain studies. *J. Nucl. Med.* 57, 136–143. <https://doi.org/10.2967/jnumed.115.156299>

Torrado-Carvajal, A., Vera-Olmos, J., Izquierdo-Garcia, D., Catalano, O.A., Morales, M.A., Margolin, J., Soricelli, A., Salvatore, M., Malpica, N., Catana, C., 2019. Dixon-VIBE Deep Learning (DIVIDE) Pseudo-CT Synthesis for Pelvis PET/MR Attenuation Correction. *J. Nucl. Med.* 60, 429–435. <https://doi.org/10.2967/jnumed.118.209288>

Tustison, N.J., Avants, B.B., Cook, P.A., Zheng, Y., Egan, A., Yushkevich, P.A., Gee, J.C., 2010. N4ITK: Improved N3 bias correction. *IEEE Trans. Med. Imaging.* 29, 1310–1320. <https://doi.org/10.1109/TMI.2010.2046908>

Wang, C., Macnaught, G., Papanastasiou, G., MacGillivray, T., Newby, D., 2018. Unsupervised learning for cross-domain medical image synthesis using deformation invariant cycle consistency networks, in: Lecture Notes in Computer Science (Including Subseries Lecture Notes in Artificial Intelligence and Lecture Notes in Bioinformatics). Springer Verlag, pp. 52–60. https://doi.org/10.1007/978-3-030-00536-8_6

Weiger, M., Pruessmann, K.P., Hennel, F., 2011. MRI with zero echo time: Hard versus sweep pulse excitation. *Magn. Reson. Med.* 66, 379–389. <https://doi.org/10.1002/mrm.22799>

Wiesinger, F., Sacolick, L.I., Menini, A., Kaushik, S.S., Ahn, S., Veit-Haibach, P., Delso, G., Shanbhag, D.D., 2016. Zero TE MR bone imaging in the head. *Magnetic Resonance in Medicine* 75, 107–114. <https://doi.org/10.1002/mrm.25545>

Wollenweber, S.D., Ambwani, S., Lonn, A.H.R., Shanbhag, D.D., Thiruvenkadam, S., Kaushik, S., Mullick, R., Qian, H., Delso, G., Wiesinger, F., 2013. Comparison of 4-class and continuous fat/water methods for whole-body, mr-based PET attenuation correction. *IEEE Trans. Nucl. Sci.* 60, 3391–3398. <https://doi.org/10.1109/TNS.2013.2278759>

Wu, Y., Ackerman, J.L., Chesler, D.A., Graham, L., Wang, Y., Glimcher, M.J., 2003. Density of organic matrix of native mineralized bone measured by water- and fat-suppressed proton projection MRI. *Magn. Reson. Med.* 50, 59–68. <https://doi.org/10.1002/mrm.10512>

Yang, H., Sun, J., Carass, A., Zhao, C., Lee, J., Xu, Z., Prince, J., 2018. Unpaired brain mr-to-ct synthesis using a structure-constrained cyclegan, in: Lecture Notes in Computer Science (Including Subseries Lecture Notes in Artificial Intelligence and Lecture Notes in Bioinformatics). Springer Verlag, pp. 174–182.
https://doi.org/10.1007/978-3-030-00889-5_20

Zhu, J.-Y., Park, T., Isola, P., Efros, A.A., 2017a. Unpaired Image-to-Image Translation using Cycle-Consistent Adversarial Networks